J Mater Sci (2015) 50:5944–5951
DOI 10.1007/s10853-015-9117-7

A simple way to synthesize anatase with high thermal stability

PengChao Wen[1] · Chao Cai[1] · Hao Zhong[1] · LuYuan Hao[1] · Xin Xu[1]

Received: 9 February 2015 / Accepted: 19 May 2015 / Published online: 17 June 2015

Abstract A simple and cost-effective method was proposed to synthesize nano-crystallized pure anatase titanium dioxide (TiO_2) photocatalysts with a high thermal stability. The initial $TiCl_4$ was reacted with a NaOH aqueous solution to form an amorphous sodium titanate, which was then transformed into an amorphous titanium dioxide hydrate through the replacement of Na^+ by H^+ using a HCl aqueous solution. After annealing, the pure nano-crystallized anatase TiO_2 particles possessed a high thermal stability up to 900 °C. The high concentration of NaOH aqueous solution played an important role in preventing the precipitation of rutile TiO_2 during hydrolysis process and promoting the formation of the nano-crystallized anatase TiO_2. Samples calcined at 800 °C exhibited a significantly higher repeatable photocatalytic activity compared to the standard commercial photocatalyst P25 for the degradation of Rhodamine B in an aqueous suspension. This could be attributed to the synergistic effect of high crystallinity and mesoporous structure. The method is very simple, template-free, and cost effective, which makes it potential for the large-scale production.

✉ Xin Xu
xuxin@ustc.edu.cn

[1] Chinese Academy of Science Key Laboratory of Materials for Energy Conversion, Department of Materials Science and Engineering, University of Science and Technology of China, Hefei 230026, People's Republic of China

Introduction

Titanium dioxide (TiO_2) has been widely studied due to its unique optical, electronic properties, and potential applications in photocatalysis, solar cells, energy conversion, chemical sensing, and so on [1–9]. Commonly, the anatase TiO_2 is more active than the other TiO_2 crystal phases, such as rutile and brookite [10, 11], and the properties of TiO_2-based materials strongly depend on their crystallinity [12]. However, because of the low anatase to rutile phase transformation temperature of ~600 °C, it is difficult to synthesize high crystalline anatase TiO_2 phase [13, 14].

Many attempts have been made to improve the thermal stability of the anatase phase TiO_2 [15–19]. Metal oxide doping and the incorporation of surface impurities were usually utilized to increase the anatase to rutile phase transformation temperature [20–23]. Zhao et al. [21] found that the formation temperature of the anatase crystallite in the mesoporous TiO_2–SiO_2 composite is greatly increased to 900 °C on account of the strong interaction between SiO_2 and TiO_2. However, those methods might have bad influence on photocatalytic activity due to the increase in charge carrier recombination centers [10, 24, 25]. Rao et al. [17] found that a solvothermal process for the amorphous TiO_2 nanotube arrays could lead to a stable anatase phase up to 800 °C, and attributed it to the increased phonon-scattering and confinement by the nanotube walls. Chen et al. [26] prepared $Na_2Ti_6O_{13}$ through the reaction between metallic Ti and NaOH in a hydrothermal condition. $Na_2Ti_6O_{13}$ was transformed into $H_2Ti_3O_7$ by the HNO_3 acid treatment, and then calcined to obtain TiO_2. However, they focused on the morphology control and the anatase to rutile transformation temperature was still as low as 450–600 °C.

In this research, a novel template-free and repeatable method was successfully employed to produce high

thermal stable and high photocatalytic effective mesoporous anatase TiO_2 from $TiCl_4$ and NaOH. The amorphous sodium titanate was selected as a precursor to obtain mesoporous nano-crystallized TiO_2. Different from other methods reported in the literatures, neither template nor hydrothermal condition is required, which leads to easy collection, mass production, low cost, and low impurities in the final products.

Experimental section

The preparation process of TiO_2

The chemical regents, such as $TiCl_4$ (≥98.0 %, C.P.), NaOH (≥96.0 %, A.R.), and HCl (36–38 %, A.R.), were all purchased from Sinopharm Chemical Regent Co., Ltd. (Shanghai, China) without further purification.

In a typical experimental process, 5 mL of $TiCl_4$ was dripped into 50 mL 5 M aqueous NaOH solution slowly under a high speed stirring and the solution was transformed into a sol. During holding at 90 °C, the sol was transformed into gel. The gel was washed repeatedly with distilled water to eliminate the redundant NaOH and impurities, such as the NaCl. The washed product was dried at 90 °C and denoted as sample A. Then 3 g sample A was suspended in 50 mL of 1 M HCl aqueous solution and vigorously stirred for 12 h to complete H^+/Na^+ ion-exchange. The product was filtered, washed, and then dried at 90 °C to obtain sample B, which was calcined in a muffle furnace at 800 °C for 2 h at a heating rate of 4 °C min^{-1}. The final product was denoted as sample C.

To have a better understanding of the method, a series of experiments has also been done with different NaOH concentrations (2 and 3.5 M) and different calcination temperatures from 500 to 1000 °C.

Characterization

The crystalline phases were identified by X-ray diffraction analysis (XRD, PW 1700, Philips Research Laboratories, Eindhoven, the Netherlands, Cu Kα1 radiation; scanning rate of 2° min^{-1}). Raman spectra were conducted on the LabRamHR (Horiba-JobinYvon, Longjumeau, French). Thermal properties were analyzed by differential thermal analysis and thermogravimetric analysis (DTA–TGA, DTG-60H, Shimadzu, Kyoto, Japan), which were conducted at a heating rate of 10 °C min^{-1} until 1200 °C.

The morphology and microstructure were observed using a field emission scanning electron microscopy (FESEM, JEOL-6390LA, JEOL, Tokyo, Japan) and a high-resolution transmission electron microscope (HRTEM, JEOL-2010, JEOL, Tokyo, Japan). An energy dispersive X-ray spectrometer (EDS) was used to analyze the elements of sample. The specific surface area and pore volume were determined from the Brunauer–Emmett–Teller (BET) and Barrett–Joyner–Halenda (BJH) reanalysis using Micromeritics Tristar II 3020M (Micromeritics, USA).

Photocatalytic assessments

The photocatalytic activity was observed by the decomposition of Rhodamine B (RhB). 0.05 g of the as-synthesized catalyst powder was added to 0.05 L of a Rhodamine B aqueous solution at a concentration of 0.01 g L^{-1} in a quartz reactor. The suspension was magnetically stirred in the dark for 30 min before illumination to establish an adsorption/desorption equilibrium between Rhodamine B and the surface of the photocatalysts. Then a 500 W Xe lamp was used as the UV and visible light source. At fixed illumination time intervals, the mixture was centrifuged to remove the catalyst particles for analysis. The concentration of Rhodamine B was analyzed with a UV–vis spectrophotometer (UV-759, Shanghai Precision & Scientific Instrument Co., Ltd., China). For comparison, the photocatalytic activity of a commercial photocatalyst Degussa P25 TiO_2 (Evonik Degussa, Germany) was also measured under the same condition.

Results and discussion

Figure 1a shows the XRD patterns of the samples A, B, and C. An amorphous phase (sample A) was obtained after the violent reaction between $TiCl_4$ and NaOH, which was accompanied by the release of a large amount of heat and smog. It was still amorphous (sample B) after HCl treatment, and transformed to the pure anatase phase (sample C) after being calcined in a muffle furnace at 800 °C for 2 h.

Figure 1b is the laser Raman spectra of the samples A, B, C, and commercial P25. Sample A exhibits six broad peaks at 282, 383, 440, 642, 703, and 905 cm^{-1}. The 282 cm^{-1}peak is attributed to the Na–O–Ti stretching vibration [27]. The 380 and 642 cm^{-1} peaks are assigned to the Ti–O bending and stretching vibration involving twofold oxygen and the 440 cm^{-1}peak is assigned to the Ti–O bending vibration involving threefold oxygen [28, 29]. The 703 cm^{-1} peak is attributed to Na–O–Ti, as reported for $Na_2O{\cdot}TiO_2$ glass [30]. The 905 cm^{-1} peak is the characteristic band of sodium titanate, which is assigned to the symmetric stretching mode of a short Ti–O bond of sodium titanate in layer structure [31]. This, along with the XRD data, implied that the sample A is an amorphous hydrate of sodium titanate (denoted as $Na_2TiO_x(OH)_{6-2x}$).

Seen from the sample B, the 905 cm^{-1} peak disappears while the 282 cm^{-1} peak of Na–O–Ti stretching vibration

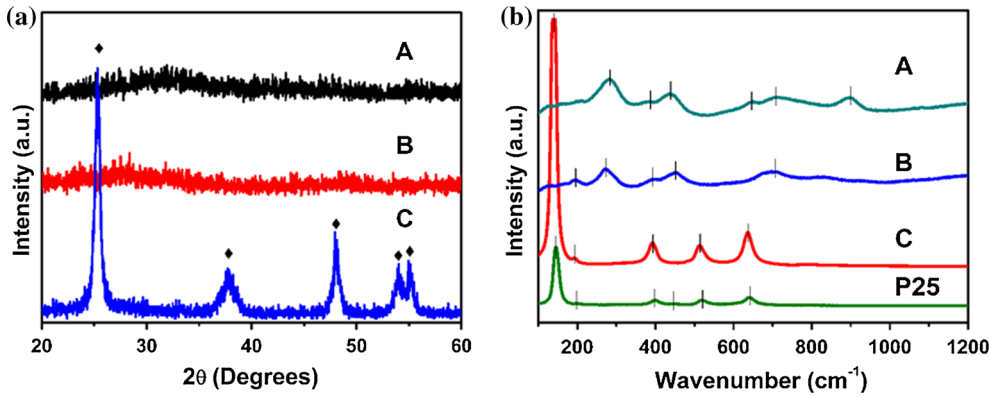

Fig. 1 **a** XRD patterns of the samples *A*, *B*, and *C*. (*filled diamond* anatase-JCPDS#21-1272); **b** Raman spectra of the samples *A*, *B*, *C*, and the commercial P25

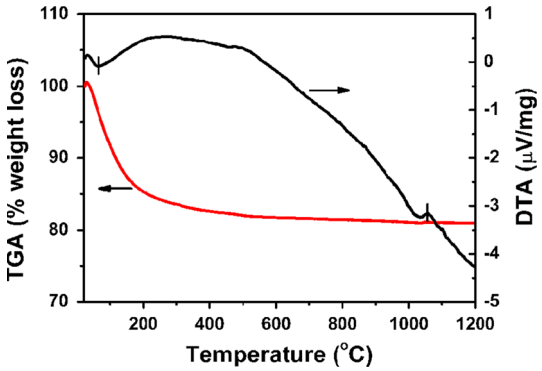

Fig. 2 DTA–TGA curve of the sample B

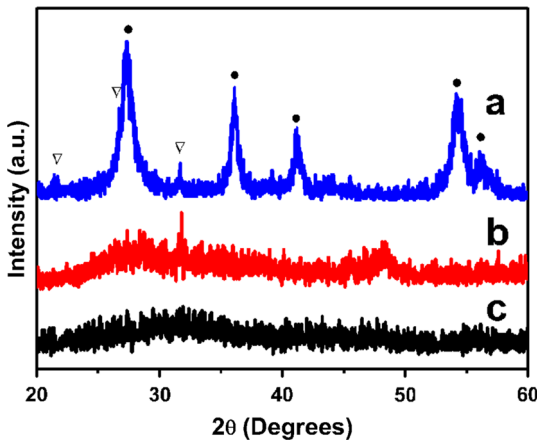

Fig. 3 XRD patterns of the sample A from different NaOH concentrations. *a–c* indicate concentration of NaOH equal 2, 3.5, 5 M. (*filled circle* rutile-JCPDS#21-1276; *open triangle* Ti_4O_7-JCPDS#72-1722)

red-shifts to 275 cm^{-1} because of the proton-exchanged reaction, indicating the removal of Na^+. The peak at 197 cm^{-1}, which is attributed to the Ti–O bonds [29], is clearly seen. This shows that sample B is an amorphous hydrate TiO_2 (denoted as $TiO_2{\cdot}yH_2O$). For sample C, the peaks at 282, 380, 440, and 703 cm^{-1} disappear, while a strong peak at 147 cm^{-1} appears. The peaks at 147, 197, 400, 520, and 642 cm^{-1} are all owing to the anatase phase TiO_2 [29].

The curve of the commercial P25 is also shown in Fig. 1, the weak peak at 445 cm^{-1} belongs to Eg phonon mode of rutile TiO_2, and all the others are attributed to the anatase TiO_2, which is consistent with the weight ratio (about 4:1) of anatase and rutile in P25. The intensity of P25 is a little lower than that of sample C, indicating that the high annealing temperature could significantly increase the crystalline.

Figure 2 shows the typical DTA–TGA thermo-diagrams of the sample B ($TiO_2{\cdot}yH_2O$). DTA analysis shows an endothermal peak below 100 °C because of the evaporation of the hydration water. The weight is drastically decreased until 300 °C and there still is little weight-loss between 300 and 1200 °C. The broad exothermic peak from 300 to 900 °C is attributed to the formation of anatase from the amorphous phase. The exothermic peak at around 1050 °C indicates the formation of rutile. The DTA–TGA curves are in good agreement with the XRD patterns.

Figure 3 shows the XRD patterns of the sample A with different NaOH concentrations of 2, 3.5, and 5 M. The rutile TiO_2 phase (JCPDS#21-1276), in company with the minor Ti_4O_7 phase (JCPDS#72-1722), can be clearly observed from 2 M NaOH. Both 3.5 and 5 M NaOH lead to the formation of an amorphous phase, except that a few Ti_4O_7 phase could also be found from 3.5 M NaOH.

The calcination temperature of the sample B ($TiO_2{\cdot}yH_2O$) might also influence the properties of the final product. Figure 4 shows the XRD patterns of sample C at different calcination temperatures of 500, 600, 700, 800, 900, and 1000 °C (denoted as T500, T600, T700, T800, T900, and T1000, respectively). Noticeably, pure anatase

TiO_2 has been obtained at a temperature as high as 900 °C. The rutile crystalline phase is formed only when the temperature reaches 1000 °C. Based on the intensity of the indicative (101) peak around 25.3°, the crystallinity is significantly increased with the increasing calcination temperature. The average dimensions of crystallites can be indicated by the width of the powder diffraction peak from the Scherrer equation (Eq. 1)

$$D = \frac{K\lambda}{B\cos\theta}, \quad (1)$$

where D is approximation of the crystallite size, K is a constant near unity, λ is the wavelength of X-ray, B is the full width at half maximum (FWHM), and θ is the angle of diffraction. Table 1 shows the calculated particle size of sample C with different calcination temperatures. The increase of the particle size with elevated temperature is due to the growth of TiO_2 crystallites.

Figure 5 shows the SEM and TEM images of T800. Figure 5a–c reveals that the TiO_2 is actually made up of small spherical particles with diameters of 8–20 nm. The sample possesses a nanoparticle-agglomerated mesoporous structure, where the nanosized grains possess an almost spherical morphology. The particles were staggeredly arranged side by side. Mesopores could be ascribed to the inter-particle space caused by the random stacking of TiO_2 nanoparticles, which could improve the absorption ability of the photocatalyst. Recently, this kind of hierarchical micro/nanostructures with high surface areas and abundant mesoporous structures has stimulated much attention [32], since such structures embrace the high dispersion and easy recovery features of micrometer-sized structures.

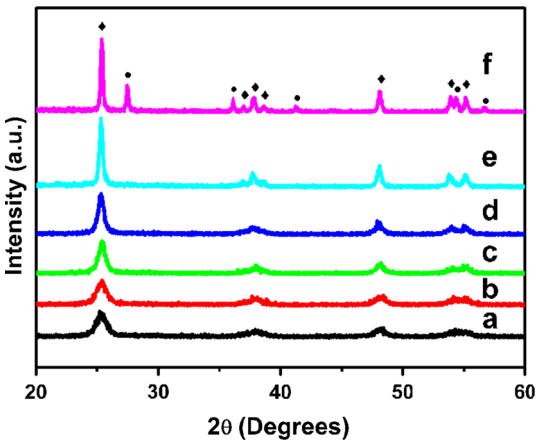

Fig. 4 XRD patterns of samples. *a* T500, *b* T600, *c* T700, *d* T800, *e* T900, and *f* T1000 (*filled diamond* anatase-JCPDS#21-1272; *filled circle* rutile-JCPDS#21-1276)

High-resolution image of Fig. 5c exhibits the 0.35 nm lattice spacing corresponding to the (101) phase of the anatase TiO_2. The selected area electron diffraction (SAED, Fig. 5d) pattern shows the polycrystalline diffraction rings corresponding to the indices of the lattice planes of the anatase phase TiO_2. From the EDS analysis, three peaks at 0.4, 4.5, 4.9 keV are attributed to Ti and the peak at 0.5 keV is O. The other peaks come from the copper substrate (0.97 and 8.0 keV) and the conducting carbon film layer (0.3 keV) is used to reduce sample charging in the electron beam. It should be noted that no dopants, including Na^+, Cl^-, has been detected, which might otherwise enhance the stability of the anatase phase.

The typical values for the specific surface area and pore volume of the samples are summarized in Table 1. With the increase of the calcination temperature, both the specific surface area and the pore volume are decreased. This could be explained by the coalescence among the grains during calcination process, leading to the collapse of small voids among particles and the increase of grain size. Figure 6 illustrates the N_2 adsorption/desorption isotherms of the sample C (T800), BJH analysis of the desorption isotherm is also shown in Fig. 6 (inset).

The sharp decline in desorption curve is indicative of the existence mesoporosity. The hysteresis between the two curves demonstrates that there is a diffusion bottle neck, possibly caused by nonuniform pore size. The pore size distribution calculated from the desorption branch of the nitrogen isotherm by the BJH method shows a narrow

Table 1 Physical properties and photocatalytic activity of the samples

Samples	Particle size (nm)	Specific surface area ($m^2\ g^{-1}$)	Pore volume ($cm^3\ g^{-1}$)	Degradation of RhB k ($min^{-1}\ g^{-1}$)
T500	19.57	167.24	0.146	0.0446
T600	21.92	128.47	0.145	0.0665
T700	23.55	107.09	0.130	0.0703
T800	26.29	64.29	0.087	0.0703
T900	35.47	4.53	0.017	0.0485
T1000	43.43	1.18	0.002	0.0237
P25	~25	46.28	0.093	0.0426

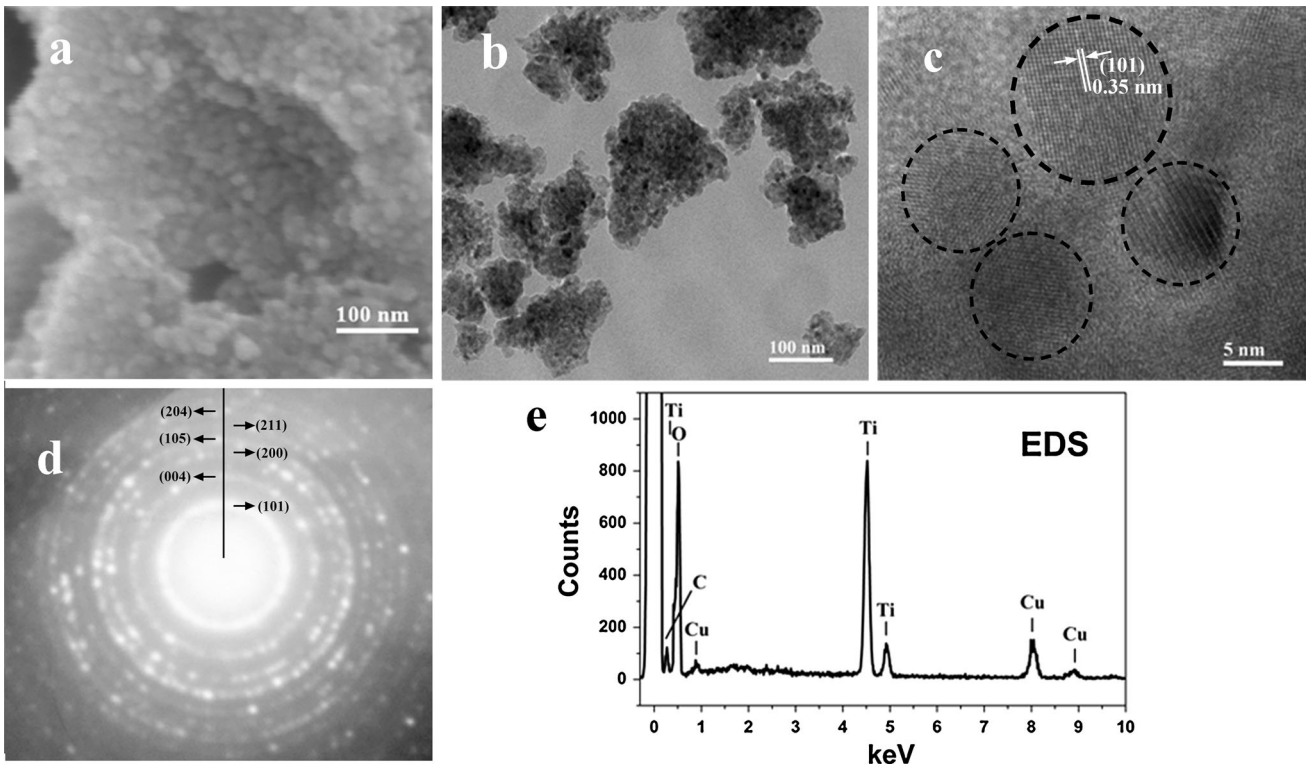

Fig. 5 SEM and TEM images of T800. **a** SEM; **b** TEM; **c** higher magnification TEM; **d** SAED; **e** EDS

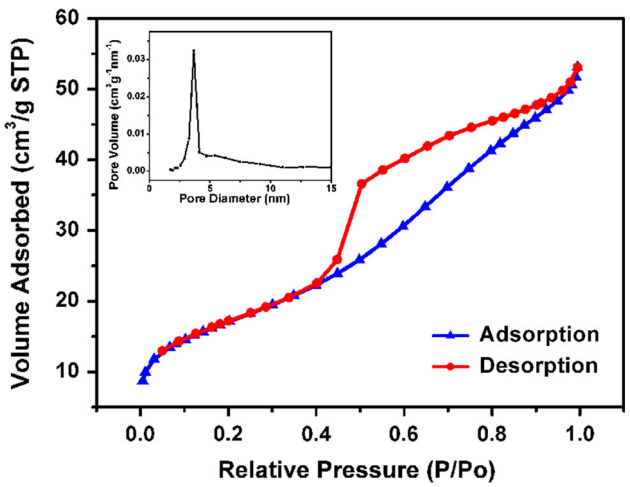

Fig. 6 N_2 adsorption/desorption isotherm and BJH pore size distribution plot (*inset*) of the sample C

range of 2.5–4.3 nm with an average pore diameter of ~3.6 nm.

Based on the experimental results mentioned above, the formation mechanism of anatase TiO_2 can be described by the Eqs. (2–5).

$$TiCl_4 + 4NaOH \rightarrow Ti(OH)_4 + 4NaCl \quad (2)$$

$$Ti(OH)_4 \rightarrow TiO_2 + H_2O \quad (3)$$

$$Ti(OH)_4 + 2OH^- \rightarrow Ti(OH)_6^{2-} \quad (4)$$

$$Ti(OH)_6^{2-} - xH_2O \rightarrow TiO_x(OH)_{6-2x}^{2-}. \quad (5)$$

When $TiCl_4$ is dripped into the NaOH solution, $Ti(OH)_4$ forms through the reaction between $TiCl_4$ and NaOH (Eq. 2), which will immediately be transformed into rutile TiO_2 precipitate (Eq. 3). The reaction is very fast that a metastable phase of Ti_4O_7 also forms on account of the inhomogeneous reaction.

However, if the concentration of NaOH is high enough, Eq. 4, instead of Eq. 3, occurs, then the electrostatic force among $Ti(OH)_6^{2-}$ ions could prevent the complete polymerization of $Ti(OH)_4$ and a steady gelation process (Eq. 5) occurs to form the gel of sample A ($Na_2TiO_x(OH)_{6-2x}$). The concentration of the NaOH aqueous solution plays a very important role in the achievement of the anatase TiO_2. The NaOH acts as an alkalinity precipitant and promotes the formation of the amorphous sodium titanate instead of the rutile TiO_2 precipitate.

Sample A ($Na_2TiO_x(OH)_{6-2x}$) is an aggregation of sodium titanium nanoparticles. When sample A was treated by the HCl, the Na^+ could be replaced by the H^+. So sample B is composed of the chaotic permutation of Ti–O

octahedrons, where numerous crystallization water and H^+ ions exist in sample B ($TiO_2{\cdot}yH_2O$).

After removing H_2O from sample B, the amorphous phase is transformed to the stable anatase phase with a high thermal stability. Li et al. [10] obtained pure and thermally stable anatase from the precursor of $K_2Ti_2O_5$, and proposed that TiO_2(B) phase in the surface was important to form the anatase crystal structure at high temperatures, however, no TiO_2(B) could be detected at any calcination temperature in our study. Padmanabhan et al. [33] has proposed a sol–gel process for the development of the high-temperature stable photoactive anatase titania, and contributed the retention of the anatase phase at 900 °C to the presence of small amounts of fluorine in the lattice. The possible influence of Cl^- could be neglected here, because pure anatase TiO_2 could also be obtained at 900 °C, if nitric acid was selected to substitute HCl.

In this study, as shown in Fig. 7, the independent $Ti(OH)_6^{2-}$ octahedral complexes are initially formed, then the condensation between the two vertex-shared octahedra leads to the formation of an edge-shared octahedra (Fig. 7a), which is followed by the linking up of a third octahedron. For the electrostatic repulsion of OH^-, the third octahedron prefers to join to the existing dioctahedra by sharing an edge (Fig. 7b), forming a zigzag structure. The structure of anatase consists of zigzag chains of octahedra, linked to each other through shared edges, while a linear chain of opposite edge-shared octahedra is found in rutile. The anatase phase could be easily formed.

In order to confirm that the third octahedron prefers to join the existing dioctahedron by sharing an edge in the high OH^- concentration, we performed first-principles calculations to compare the theoretical energy of different connections [34, 35]. Based on the $Ti(OH)_6^{2-}$ octahedron, we constructed two $Ti_3(OH)_{14}^{2-}$ clusters, one is the linear chain of octahedron corresponding to rutile (Fig. 7c), and the other is the zigzag chains of octahedron corresponding to anatase (Fig. 7d).

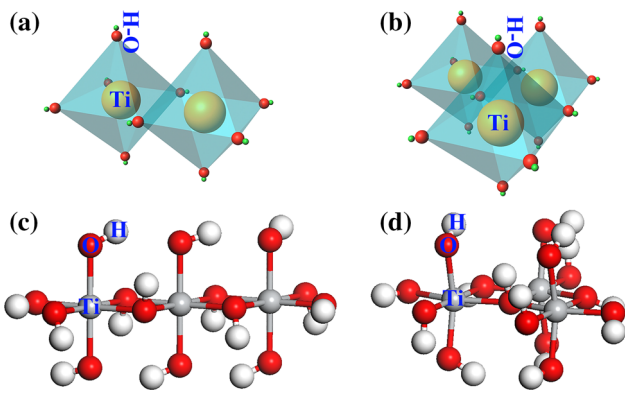

Fig. 7 Scheme of the phase transformation and the structure of Ti–OH octahedral. **a** and **b** are the scheme of the phase transformation from amorphous to anatase; **c** is the linear chain of octahedron corresponding to rutile; **d** is the zigzag chain of octahedron corresponding to anatase

For these two clusters, the energy was performed using the CASTEP code. A plane wave basis set with kinetic energy cutoff at 680 eV was employed, and the Perdew–Burke–Ernzerhof form of the generalized gradient approximation (GGA) was used to describe the exchange–correlation interactions, while the electron–ion interaction was accounted for the use of ultrasoft pseudopotentials. The detailed parameters were chosen as follows: *k*-point spacing = 0.057 $Å^{-1}$, sets of *k* points = 1×1 × 1, space representation = reciprocal, and SCF tolerance threshold = 2.0×10^{-6} eV/atom.

The energies of Fig. 7c, d are −11165.3043 and −11167.5497 eV, respectively. The energy of the linear chain of opposite edge-shared octahedron is much higher than that of the zigzag chain of octahedron. This indicates that the formation of zigzag chain is thermodynamically conducive in the high OH^- concentration.

It was reported that the anatase phase is stable with an average size below 30 nm [17]. The high OH^- concentration could also prevent the growth of the $Ti(OH)_6^{2-}$ cluster due to the electrostatic repulsion of OH^-, which leads to small sodium titanium nanoparticles in sample A. The large amount of hydration water and H^+ ions in sample B, just like surface impurities, could inhibit crystal growth and then suppress the phase transformation from anatase to rutile [36].

The photocatalytic activities for our obtained TiO_2 were evaluated by the degradation of RhB aqueous solution under UV–vis light irradiation by a 500 W Xe lamp. Figure 8a shows the photocatalytic degradation of RhB as a function of time for commercial P25 and our obtained TiO_2. The kinetics of RhB photodegradations over each of the samples and P25 were investigated, from which the apparent reaction rate constants *k* have been calculated. For each sample, *k* was obtained by plotting $\ln(C_0/C)$ as a function of time *t* and weight of photocatalyst *g* (Table 1, column of degradation of RhB). A higher value of *k* for a particular catalyst means that it has a higher activity for photodegradation of organics which enables us to quantitatively determine the photocatalytic activities of the different catalysts.

Before turning on the illuminant, the photocatalyst suspension was placed in the dark for 30 min in order to establish an adsorption/desorption equilibrium between RhB and the surface of the photocatalysts. The adsorption amount of RhB on the obtained nanosized porous anatase is higher than P25 owing to the existence of

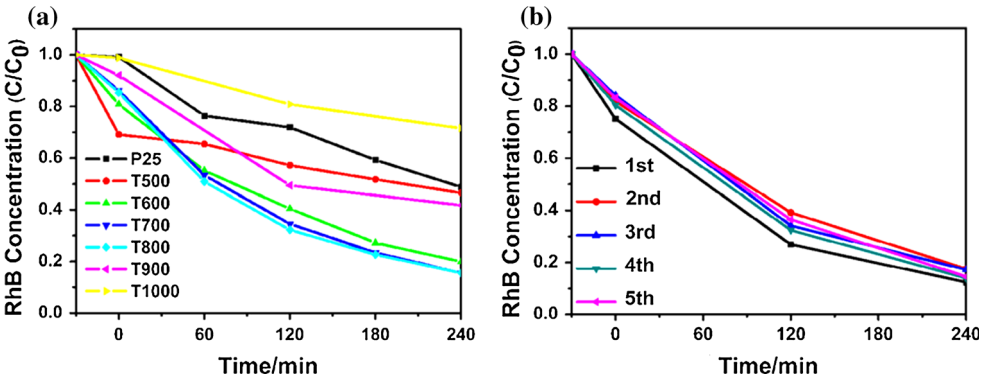

Fig. 8 The photocatalytic degradation of RhB for different samples and the repeated photocatalytic activities for the degradation of RhB. C_0 is the concentration of the original solution of RhB, C is the result concentration of RhB after being degraded by photocatalyst

many mesopores between grains. With the increase of the calcination temperature, the adsorption amount of RhB is decreased, which agrees with the decrease in the surface area and pore volume.

After light on, the concentration of RhB exhibits further decrease. Despite its highest surface accessibility (high surface areas and pore volume), T500 shows slower decomposition rate and catalytic property, which could be attributed to its lower anatase crystallinity. The sample with a low crystalline contains a large number of lattice defects, which act as recombination centers of electron–hole pairs [10]. Samples T600–T800 all exhibit higher photocatalytic activities than P25 and the highest activity could be achieved for T800. We can see the same result from k value in Table 1. The enhanced activity of T600 could be attributed to the higher surface areas and pore volumes, which could increase the catalytic sites to degrade the molecules under UV–vis light irradiation; while the remarkably enhanced activity of T800 is related to the enhanced crystallinity, which could reduce the number of lattice defect sites that act as recombination centers for electron–hole pairs [37]. The high thermal stability enables to achieve elevated photocatalytic activity by increasing the crystallinity. With the further increasing calcination temperature to 900 and 1000 °C, nanoparticles tend to aggregate, the mesoporous structures between particles gradually disappear, and the phase transformation from anatase to rutile is triggered. All of these phenomena are detrimental to the photocatalytic activity. The catalytic property depends on the bifunctional effect of the crystalline anatase nanoparticles and surface area (pore volume).

The maintenance of high photocatalytic activity in cycling use is a critical issue for long-term applications. Figure 8b exhibits the repeated photocatalytic activities of T800. There is no obvious decrease in the photocatalytic activity through the test times, which indicates that the obtained anatase has a good long-term stability.

Conclusions

Pure nano-crystallized anatase TiO_2 with a high thermal stability and a good photocatalytic activity has been prepared. The high NaOH concentration plays an important role in the method. The thermal stable TiO_2 can be synthesized only if the concentration of NaOH is high enough in the initial reaction, which could be partially confirmed by the first-principles calculations. The crystallinity and phase composition of the samples show great influence on the photocatalytic activity. The experiment results indicate that pure stable anatase TiO_2 with a high photocatalytic effectivity could be achieved, when the concentration of NaOH was 5 M and the heat-treating temperature was 800 °C. This method is very simple, moderate, seedless, template-free, and cost effective, making it potential for the large-scale production.

Acknowledgements This research was supported by the National Natural Science Foundation of China (Grant No. 51072191, 11179037), National Basic Research Program of China (973 Program, 2012CB922004).

References

1. Zhang R, Elzatahry AA, Al-Deyab SS, Zhao D (2012) Mesoporous titania: from synthesis to application. Nano Today 7:344–366
2. Froschl T, Hormann U, Kubiak P, Kucerova G, Pfanzelt M, Weiss CK, Behm RJ, Husing N et al (2012) High surface area crystalline titanium dioxide: potential and limits in electrochemical energy storage and catalysis. Chem Soc Rev 41:5313–5360
3. Bumajdad A, Madkour M, Abdel-Moneam Y, El-Kemary M (2013) Nanostructured mesoporous Au/TiO_2 for photocatalytic degradation of a textile dye: the effect of size similarity of the deposited Au with that of TiO_2 pores. J Mater Sci 49:1743–1754. doi:10.1007/s10853-013-7861-0
4. Ni M, Leung MKH, Leung DYC, Sumathy K (2007) A review and recent developments in photocatalytic water-splitting using TiO_2 for hydrogen production. Renew Sustain Energy Rev 11:401–425
5. Arun TA, Chacko DK, Madhavan AA, Deepak TG, Anjusree GS, Sara T, Ramakrishna S, Nair SV et al (2014) Flower-shaped

anatase TiO_2 mesostructures with excellent photocatalytic properties. RSC Adv 4:1421–1424
6. Nair AS, Yang SY, Zhu PN, Ramakrishna S (2010) Rice grain-shaped TiO_2 mesostructures by electrospinning for dye-sensitized solar cells. Chem Commun 46:7421–7423
7. Ganesh VA, Raut HK, Nair AS, Ramakrishna S (2011) A review on self-cleaning coatings. J Mater Chem 21:16304–16322
8. Di Lupo F, Tuel A, Mendez V, Francia C, Meligrana G, Bodoardo S, Gerbaldi C (2014) Mesoporous TiO_2 nanocrystals produced by a fast hydrolytic process as high-rate long-lasting Li-ion battery anodes. Acta Mater 69:60–67
9. Colmenares-Angulo JR, Cannillo V, Lusvarghi L, Sola A, Sampath S (2008) Role of process type and process conditions on phase content and physical properties of thermal sprayed TiO_2 coatings. J Mater Sci 44:2276–2287. doi:10.1007/s10853-008-3044-9
10. Li W, Bai Y, Liu C, Yang ZH, Feng X, Lu XH, van der Laak NK, Chan KY (2009) Highly thermal stable and highly crystalline anatase TiO_2 for photocatalysis. Environ Sci Technol 43:5423–5428
11. Ovenstone J, Yanagisawa K (1999) Effect of hydrothermal treatment of amorphous titania on the phase change from anatase to rutile during calcination. Chem Mater 11:2770–2774
12. Kawahara T, Konishi Y, Tada H, Tohge N, Nishii J, Ito S (2002) A patterned TiO_2(anatase)/TiO_2(rutile) bilayer-type photocatalyst: effect of the anatase/rutile junction on the photocatalytic activity. Angew Chem Int Ed 41:2811–2813
13. Dhage SR, Pasricha R, Ravi V (2003) Synthesis of ultrafine TiO_2 by citrate gel method. Mater Res Bull 38:1623–1628
14. Huang PJ, Chang H, Yeh CT, Tsai CW (1997) Phase transformation of TiO_2 monitored by thermo-Raman spectroscopy with TGA/DTA. Thermochim Acta 297:85–92
15. Kominami H, Takada Y, Yamagiwa H, Kera Y, Inoue M, Inui T (1996) Synthesis of thermally stable nanocrystalline anatase by high-temperature hydrolysis of titanium alkoxide with water dissolved in organic solvent from gas phase. J Mater Sci Lett 15:197–200
16. Schliesser JM, Smith SJ, Li G et al (2015) Heat capacity and thermodynamic functions of nano-TiO_2 anatase in relation to bulk-TiO_2 anatase. J Chem Thermodyn 81:298–310
17. Rao BM, Roy SC (2014) Anatase TiO_2 nanotube arrays with high temperature stability. Rsc Adv 4:38133–38139
18. Hanaor DAH, Sorrell CC (2010) Review of the anatase to rutile phase transformation. J Mater Sci 46:855–874. doi:10.1007/s10853-010-5113-0
19. Zhou W, Sun F, Pan K, Tian G, Jiang B, Ren Z, Tian C, Fu H (2011) Well-ordered large-pore mesoporous anatase TiO_2 with remarkably high thermal stability and improved crystallinity: preparation, characterization, and photocatalytic performance. Adv Funct Mater 21:1922–1930
20. Chen WB, Ma ZJ, Pan XZ, Hu ZL, Dong GP, Zhou SF, Peng MY, Qiu JR (2014) Core@dual-shell nanoporous SiO_2-TiO_2 composite fibers with high flexibility and its photocatalytic activity. J Am Ceram Soc 97:1944–1951
21. Dong WY, Sun YJ, Lee CW, Hua WM, Lu XC, Shi YF, Zhang SC, Chen JM, Zhao Dongyuan (2007) Controllable and repeatable synthesis of thermally stable anatase nanocrystal-silica composites with highly ordered hexagonal mesostructures. J Am Chem Soc 129:13894–13904
22. Reidy DJ, Holmes JD, Nagle C, Morris MA (2005) A highly thermally stable anatase phase prepared by doping with zirconia and silica coupled to a mesoporous type synthesis technique. J Mater Chem 15:3494–3500
23. Gennari FC, Pasquevich DM (1998) Kinetics of the anatase rutile transformation in TiO_2 in the presence of Fe_2O_3. J Mater Sci 33:1571–1578. doi:10.1023/A:1017515804370
24. Xie TH, Lin J (2007) Origin of photocatalytic deactivation of TiO_2 film coated on ceramic substrate. J Phys Chem C 111:9968–9974
25. Nam HJ, Amemiya T, Murabayashi M, Toh K (2004) Photocatalytic activity of sol-gel TiO_2 thin films on various kinds of glass substrates: the effects of Na^+ and primary particle size. J Phys Chem B 108:8254–8259
26. Peng X, Chen A (2006) Large-scale synthesis and characterization of TiO_2-based nanostructures on Ti substrates. Adv Funct Mater 16:1355–1362
27. Liu H, Yang D, Zheng Z, Ke X, Waclawik E, Zhu H, Frost RL (2010) A Raman spectroscopic and TEM study on the structural evolution of $Na_2Ti_3O_7$ during the transition to $Na_2Ti_6O_{13}$. J Raman Spectrosc 41:1331–1337
28. Kim HM, Miyaji F, Kokubo T, Nakamura T (1997) Effect of heat treatment on apatite-forming ability of Ti metal induced by alkali treatment. J Mater Sci 8:341–347. doi:10.1023/A:1018524731409
29. Ocana M, Garciaramos JV, Serna CJ (1992) Low-temperature nucleation of rutile observed by Raman-spectroscopy during crystallization of TiO_2. J Am Ceram Soc 75:2010–2012
30. Kasuga T, Hiramatsu M, Hoson A, Sekino T, Niihara K (1999) Titania nanotubes prepared by chemical processing. Adv Mater 11:1307–1311
31. Byeon SH, Lee SO, Kim H (1997) Structure and Raman spectra of layered titanium oxides. J Solid State Chem 130:110–116
32. Li J, Wang GZ, Wang HQ, Tang CJ, Wang YQ, Liang CH, Cai WP, Zhang LD (2009) In situ self-assembly synthesis and photocatalytic performance of hierarchical $Bi_{0.5}Na_{0.5}TiO_3$ micro/nanostructures. J Mater Chem 19:2253–2258
33. Padmanabhan SC, Pillai SC, Colreavy J, Balakrishnan S, McCormack DE, Perova TS, Gun'ko Y, Hinder SJ, Kelly JM (2007) A simple sol-gel processing for the development of high-temperature stable photoactive anatase titania. Chem Mater 19:4474–4481
34. Ji W, Lee MH, Hao LY, Xu X, Agathopoulos S, Zheng D, Fang C (2015) Role of oxygen vacancy on the photoluminescence of $BaMgSiO_4$: Eu phosphors: experimental and theoretical analysis. Inorg Chem 54:1556–1562
35. Ju LC, Xu X, Hao LY, Lin Y, Lee MH (2015) Modification of the coordination environment of Eu^{2+} in Sr_2SiO_4: Eu^{2+} phosphors to achieve full color emission. J Mater Chem C 3:1567–1575
36. Chen B, Zhang HZ, Gilbert B, Banfield JF (2007) Mechanism of inhibition of nanoparticle growth and phase transformation by surface impurities. Phys Rev Lett 98:10613
37. Furube A, Asahi T, Masuhara H, Yamashita H, Anpo M (1999) Charge carrier dynamics of standard TiO_2 catalysts revealed by femtosecond diffuse reflectance spectroscopy. J Phys Chem B 103:3120–3127